Interplay between exchange-split Dirac and Rashba-type surface states at the $MnBi_2Te_4$/BiTeI interface

N. L. Zaitsev,[1] I. P. Rusinov,[2] T. V. Menshchikova,[2] and E. V. Chulkov[3,4,5,2]

[1]*Institute of Molecule and Crystal Physics, Subdivision of the Ufa Federal Research Centre of the Russian Academy of Sciences, 450075, Ufa, Russia*

[2]*Laboratory of Nanostructured Surfaces and Coatings, Tomsk State University, 634050 Tomsk, Russia*

[3]*Laboratory of Electronic and Spin Structure of Nanosystems, Saint Petersburg State University, 198504 Saint Petersburg, Russia*

[4]*Departamento de Polímeros y Materiales Avanzados: Física, Química y Tecnología, Facultad de Ciencias Químicas, Universidad del País Vasco UPV/EHU, 20080 Donostia-San Sebastián, Basque Country, Spain*

[5]*Donostia International Physics Center (DIPC), 20018 Donostia-San Sebastián, Basque Country, Spain*

(Received 11 August 2022; accepted 21 December 2022; published 3 January 2023)

Based on *ab initio* calculations, we study the electronic structure of the BiTeI/$MnBi_2Te_4$ heterostructure interface composed of the antiferromagnetic topological insulator $MnBi_2Te_4$ and the polar semiconductor trilayer BiTeI. We found a significant difference in the electronic properties of the different contacts between the substrate and overlayer. While the case of a Te-Te interface forms a natural expansion of the substrate, when the Dirac cone state locates mostly in the polar overlayer region and undergoes a slight exchange splitting, the Te-I contact is the source of a four-band state contributed by the substrate Dirac cone and Rashba-type state of the polar trilayer. Owing to magnetic proximity, the pair of Kramers degeneracies for this state is lifted, which produces a Hall response in the transport regime. We believe our findings provide new opportunities to construct novel spintronic devices.

DOI: 10.1103/PhysRevB.107.045402

I. INTRODUCTION

The interplay between the spin-orbit interactions and magnetism attracts a lot of attention owing to the impact on the band topology and electron transport phenomena [1–3]. In the case of asymmetric bulk and surface systems, the spin-orbit effects produce the Rashba spin splitting of bulk and surface bands [4,5], which is exploited in the proposed spin-field transistor [6,7]. Another example is the quantum spin Hall effect reflected in the formation of Dirac cone states with the "spin filtering" transport property on the boundaries of topological insulators (TIs) [8]. The introduction of magnetism enriches the complexity and noteworthiness of the systems with the mentioned spin-orbital phenomena via the breaking time-reversal symmetry and thus lifting degeneracies of the Rashba states and Dirac cones. It forms an additional topological band gap which is the source of the spin-based transport phenomena like the recently proposed chiral orbital magnetization effect [9], which allows applying such systems in spintronic devices [7,10,11] and quantum computation [12,13].

One possible strategy of further research of interrelation between magnetic and spin-orbit effects is based on the design of complex heterostructures with both these contributions. Owing to the weak chemical interaction between building blocks, the van der Waals compounds provide a suitable platform to design systems with the desired properties [14,15] via the molecular beam epitaxy or mechanical exfoliation techniques [16].

The ideal ingredients for a design of complex heterostructures with both magnetic and spin-orbital effects are the antiferromagnetic topological insulator $MnBi_2Te_4$ and polar semiconductor BiTeI. The former is a magnetic semiconductor [17] composed of the seven-layer (7L) blocks coupled by Van der Waals forces along the [0001] direction. This magnetic topological insulator has been proposed as an efficient platform for magnetic spintronics [18–23], containing exchange-split bands on the (0001) cleavage plane and providing the effect of magnetic proximity. Another constituent, the polar semiconductor BiTeI, is built up by polar trilayers and is characterized by the giant Rashba-type spin splitting of both bulk gap edge and surface states [24,25]. The excellent match of the in-plane crystal cell parameters for both constituents prevents dislocations or the Moiré pattern effects during the formation of the interface.

Here, we report a density functional theory (DFT) study of the van der Waals heterostructure composed by the antiferromagnetic topological insulator $MnBi_2Te_4$(0001) surface (MBT) and polar semiconductor BiTeI trilayer resulting in the formation of the BiTeI/MBT interface. The Te–Te contact case forms a nonmagnetic extension of an $MnBi_2Te_4$ pristine surface by a BiTeI trilayer, which is expressed in a spatial shifting of the exchange-split Dirac cone surface state into the overlayer region. This behavior is caused by a strong spin-orbit contribution in both the substrate and overlayer and by the absence of strong perturbation of the electrostatic potential over the BiTeI trilayer deposition. Also it is accompanied by the shrinking of the exchange band gap of the Dirac cone and its downward shifting at overlayer deposition.

In the case of the Te–I contact, the energy spectrum near the Fermi level is formed by a four-band state composed by the Rashba-type state of the overlayer and Dirac state of the

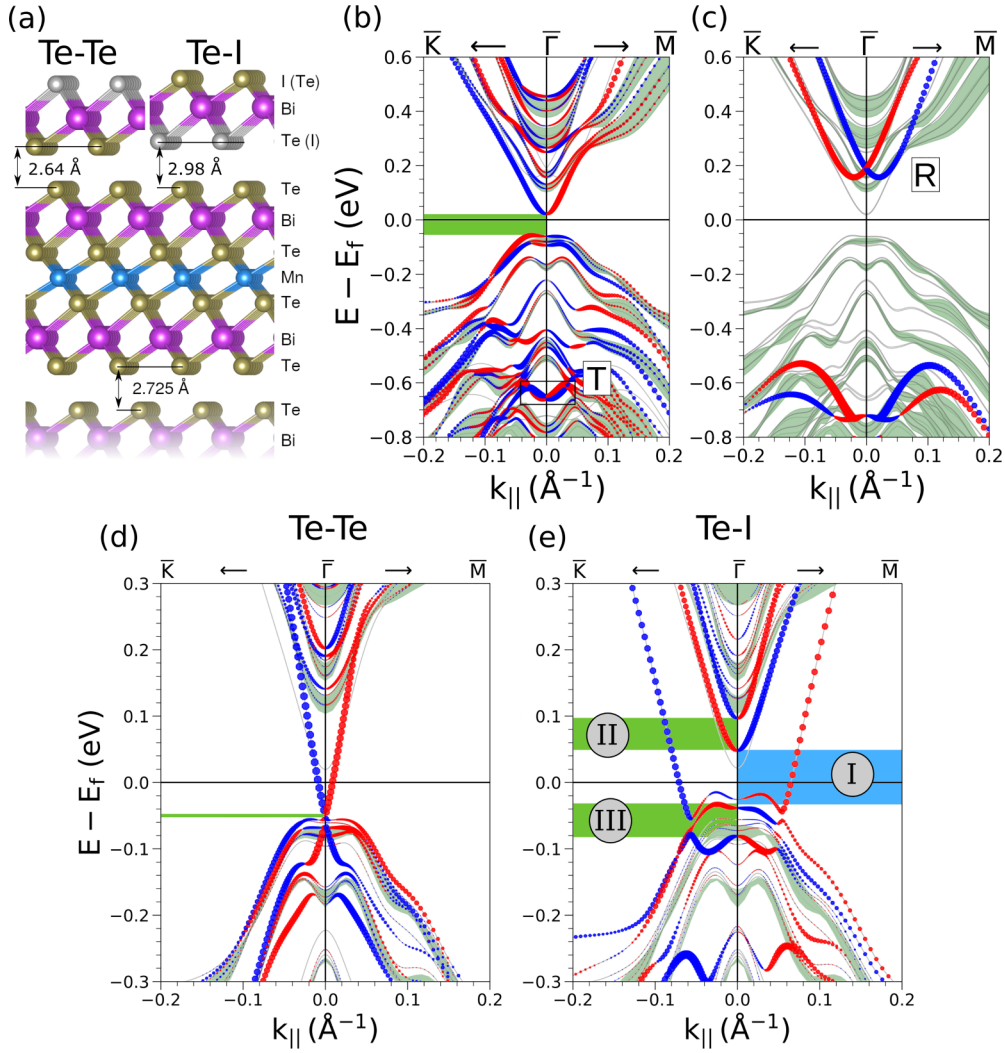

FIG. 1. (a) Schematic geometrical structure of the BiTeI/MBT interface with different orientations of the BiTeI trilayer. In-plane spin-resolved surface band structure calculated with large separation of 12 Å between the (b) pristine $MnBi_2Te_4$ (0001) surface and (c) BiTeI trilayer. Spin-resolved electron spectrum for (d) Te-Te and (e) Te-I interfaces in the case of equilibrium structures. The value and direction of the in-plane spin projection are coded by the circle size and color, where the positive value corresponds to red and the negative to blue. The light green area represents bulk projected bands, and the black rectangular emphasizes the trivial surface states of $MnBi_2Te_4$(0001). For (b), (d), and (e), the magnetic exchange and hybridization energy gap at the center of SBZ are denoted by green (blue) rectangles. In (e), the hybridization energy gap is denoted as I and two exchange gaps as II and III. In (c) and (d), the unoccupied Rashba states are denoted by the R symbol. The trivial surface states of the MBT are shown by the T symbol.

magnetic substrate surface. In the vicinity of the Brillouin zone center, there are two types of features: (1) a hybridized band gap, owing to interaction of these two states, and (2) two exchange gaps, owing to magnetic proximity with the substrate. The latter features are the source of intrinsic Hall conductivity, due to time-reversal symmetry breaking, what allows applying this state in spintronic devices. This finding demonstrates another way to form a hybridization gap between the Rashba-type and Dirac cone states, which is also previously observed in pristine MBT [26] and $MnBi_6Te_{10}$ [27] surfaces.

II. CALCULATION DETAILS

The crystal structure of $MnBi_2Te_4$ is characterized by the lattice parameters $a = 4.33$ Å and $c = 40.93$ Å [28]. The same a parameter is used for BiTeI trilayer placed on top of MBT [Fig. 1(a)]. The semi-infinite MBT was represented by periodically repeated slabs of six septuple layers in width, with vacuum imposed in z direction along the surface normal. The BiTeI trilayer was attached to one side of the slab. The effective screening medium method [29] was used for proper matching of the potential in the vacuum region of the asymmetric slab. Both parallel and antiparallel aligning of the $MnBi_2Te_4$(0001) surface normal with the BiTeI trilayer dipole moment (directed towards the Te layer) was considered. Hereinafter, we denote these two cases as Te–I and Te–Te interfaces [see Fig. 1(a)]. We considered a type of junction between the substrate and the overlayer that is similar to the one between the adjacent seven-layer blocks inside the MBT substrate.

The equilibrium vertical separation d_0 between MBT and the trilayer was determined from relaxation of interplanar distances of the utter MBT septuple layer along with BiTeI, whereas the rest of the slab was fixed in the bulk geometry. The structural optimization was performed within the PBE-D3 scheme [30,31], which incorporates an empirical correction to include dispersion forces on top of the PBE functional using the projector augmented-wave (PAW) method [32,33] implemented in VASP [34]. The Hamiltonian contained scalar relativistic corrections, and the spin-orbit coupling (SOC) was taken into account [35,36]. We used the PAW pseudopotentials with 5 (Bi), 6 (Te), 7 (I), and 7 (Mn) valence electrons. As it turned out, the influence of spin-orbit coupling on the force field is quite noticeable. The elongation of the equilibrium vertical separation d_0 due to SOC reaches 0.1 Å in case of the Te-I interface providing $d_0 = 2.98$ Å, while it is half as much for the Te-Te case with $d_0 = 2.64$ Å (see Table 1 in Ref. [44]). Therefore all electronic structure results were obtained for geometries optimized with inclusion of SOC. Note that the variation of interplanar atomic distances within atomic blocks has no significant effect on the surface electronic bands rearrangement.

Ab initio electronic structure calculations were performed within the DFT as implemented in the OPENMX (version 3.8) code [37]. The linear combination of localized pseudoatomic orbitals [38–40] was used to construct the basis functions. The fully relativistic norm-conserving pseudopotential [41] which incorporates SOC contribution [42] was taken as a replacement for the deep core potential. The generalized gradient approximation Perdew-Burke-Ernzerhof (PBE) functional [43] was applied for the exchange-correlation energy. The basis functions were set as follows: Mn6.0-*s3p3d2*, Te(I)7.0-*s3p3d2f1*, and Bi8.0-*s3p3d2f1*, namely, 3 primitive orbitals for each *s* and *p* channels and 2 primitive orbitals for the *d* channel with the cutoff radius of 6.0 a.u. were used to define Mn atoms, etc. The pseudopotentials of Bi, Te, I, and Mn have comprised 15, 16, 7, and 15 valence electrons, respectively. The real-space grid for numerical integration and solution of the Poisson equation was set to 200 Ry of the cutoff energy. The total energy convergence criterion was 3×10^{-5} eV. The surface Brillouin zone (SBZ) of the supercell was sampled with a 7×7 mesh of **k** points, which is sufficient to achieve reasonable accuracy of the calculations (see Figs. 1(b) and 1(c) in Ref. [44]).

The calculated in-plane spin-resolved band structure of BiTeI/MBT interface with the 12-Å separation between the MBT surface and the BiTeI trilayer (to eliminate any interactions between them) is shown in Figs 1(b) and 1(c). The panels depict the bands localized within the surface septuple layer of MBT [Fig. 1(b)] and within the BiTeI trilayer [Fig. 1(c)], respectively. In contrast to the nonmagnetic case of the structurally similar $PbBi_2Te_4$ and $PbSb_2Te_4$ surfaces, where Kramers degeneracies are located within the projected band gap [45,46], the presence of a magnetic exchange field of MBT lifts this degeneracy in topological surface states (TSS), which forms the gap of ∼80 meV [Fig. 1(b)]. Thus the upper part of the Dirac cone lies within the projected band gap above the Fermi level, whereas the lower part with a flattened vertex resides just above the valence band [17,47–49]. The formation of an exchange gap also triggers the S_z spin contribution in this part of the spectrum (see also the *ab initio* spectra presented in Ref. [17]). Note that at an energy of ~ -0.65 eV, there are trivial surface states (SS) of MBT [Fig. 1(b)], which are heavily involved into interaction with BiTeI, as will be seen further. In turn, the degenerate point of the highly split Rashba state of the BiTeI trilayer lies above the Fermi level and moreover overlaps with the bulk projected bands of MBT [Fig. 1(c)].

III. RESULTS

The relaxed Te-Te and Te-I interfaces have similar values of total energy, where the first one is 0.1 eV more favorable than the second one. Also, the first interface is characterized by the ∼0.3 Å shorter interlayer distance between trilayer and MBT (Te-Te interface spacing $d_0 = 2.64$ Å, Te-I: $d_0 = 2.98$ Å) and is a bit shorter than the vdW spacing of MBT substrate ($d_{vdW} = 2.725$ Å) [see also Fig. 1(a)]. The other interplane distances are tolerant to the interface type.

The *ab initio* spin-resolved surface electronic spectrum of Te-Te interface [Fig. 1(d)] has notable changes with respect to the pristine MBT surface [Fig. 1(b)] and nonmagnetic $BiTeI/PbSb_2Te_4$ interface with the same layer stacking [45]. Namely, a tiny exchange Dirac gap [see green rectangle in Fig. 1(d)] of a few meV width takes place, located just above the valence band maximum. The shifted down Dirac state has increased velocity. With that, at the SBZ center, the lower part of the Dirac cone overlaps with the set of weak surface states inherited from the highest MBT bulk valence state, due to the electrostatic field near the surface. In turn, the Rashba-type state resides at ∼0.2 eV lessening their momentum splitting. Note that the BiTeI overlayer on MBT is prone to pull the surface states into itself, like in the case of adsorption on Au(111) [50] or $PbSb_2Te_4(0001)$ [45] surfaces.

Other trends can be seen in the electronic structure of the Te-I interface [see Fig. 1(e)]. In the area near the Fermi level, a set of spin-polarized states appears. As will be discussed afterwards in detail, they are separated by energy gaps of different nature. The two gaps (II and III) [green color rectangles] are of exchange type and are originated from the presence of a magnetic MBT substrate. The highest (lowest) exchange gap is of ∼49 meV (of ∼42 meV) width. Another type gap (I) is crossed by the Fermi level and is of ∼86 meV width (blue color rectangle). It has a hybridization character and is induced by interaction of the surface cone state of MBT and the Rashba-type state of the overlayer. The gap of same nature has been observed previously at consideration of the nonmagnetic $BiTeI/PbSb_2Te_4$ surface heterostructure [45]. In such a way, Te-I interface forms the single four-band state composed of the two-band Dirac and Rashba-type states. Out of the area of the SBZ center, where the hybridization gap is formed, the discussed four-band state dispersion is inherited from these spin-orbit contributions. To provide additional evidence for nature of the presented gaps, we have calculated surface electronic structure with magnetic easy direction along the in-plane axis (see Fig. 3 in Ref. [44]). In this case, the exchange gaps II and III shrink to zero, similar as it happens for the Dirac point on the surface of magnetically doped topological insulators [51] or V-based antiferromagnetic topological insulators [52], while the hybridization gap remains unchanged.

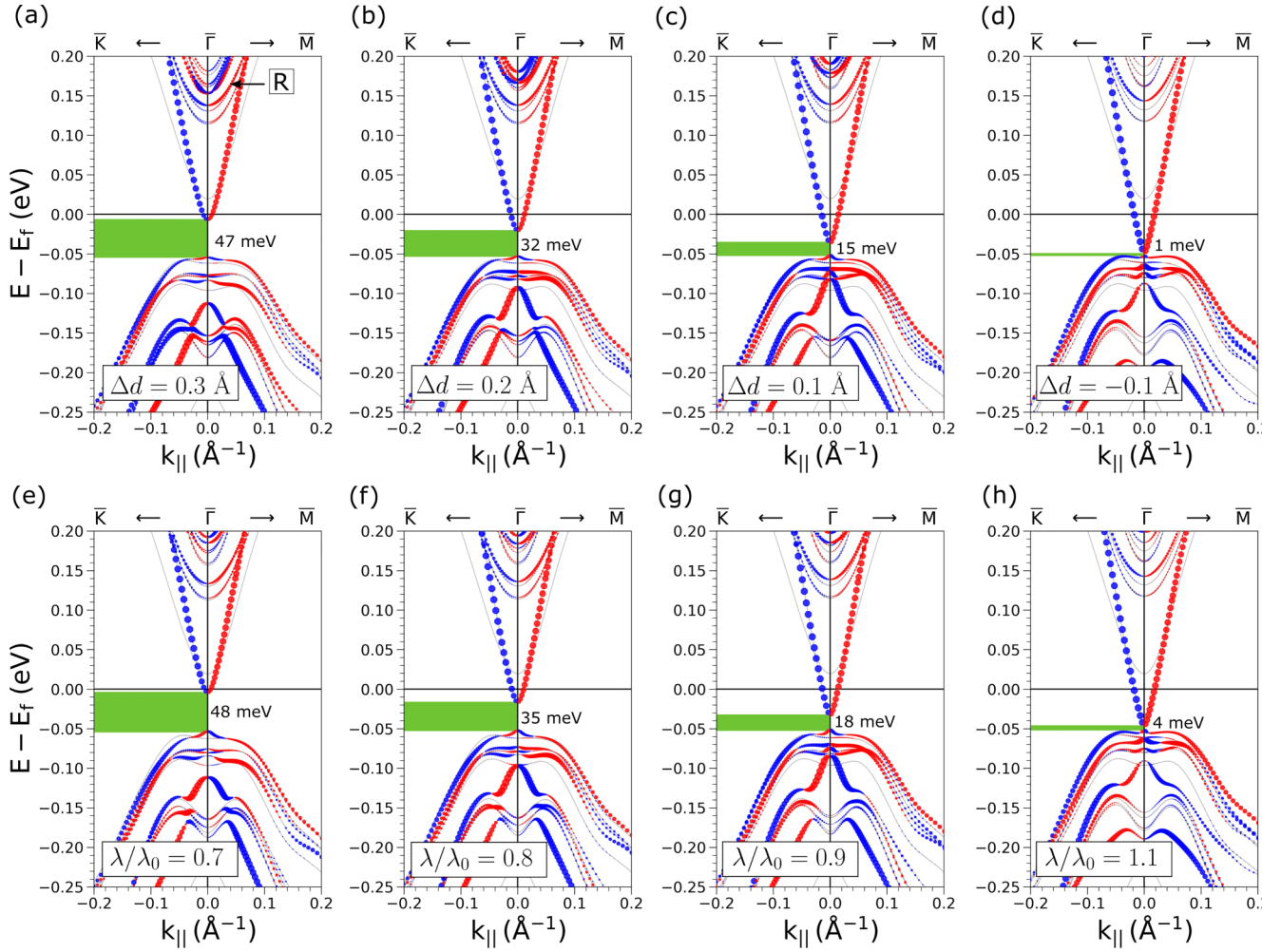

FIG. 2. Surface spin-resolved electronic structure of a Te–Te interface [(a)–(d)] for different separations between the MBT surface and trilayer with respect to the equilibrium geometry, $\Delta d = d - d_0$, and [(e)–(h)] for a different spin-orbit coupling strength of the Bi and Te p states of BiTeI trilayer. The natural SOC contribution gives $\lambda/\lambda_0 = 1$. In the panels, the magnetic exchange gap at the SBZ center is indicated by the green areas. For each panel, the gap width is denoted from the right side of the green area. In (a), the subsurface Rashba state is denoted by the R symbol.

It should be noted that due to presence of the valence band maximum which plays a role of charge reservoir, the potential gradient near the surface region produces additional surface states which are involved in the interaction with the four-band state under consideration, which can be regarded as the simplification of the low-energy surface electronic spectrum for this type of interface.

A. Te–Te interface

The origins of the calculated electronic structure of the equilibrium Te-Te interface can be clarified by varying the vertical separation d between MBT and polar trilayer, which changes the interaction between these building blocks. Also, electronic spectra at an increased d correspond to the cases when additional species intercalate into the van der Waals region inert atoms. The examples are atomic clusters or molecules with ion-covalent bonding confined within these species [46,47,53]. The effect of expanding the interlayer distance has also been studied experimentally in some van der Waals materials like MoS_2 [54,55].

At $d = 3.24$ Å, the interaction between the substrate and overlayer is rather weak [see Fig. 3(a)], and the bands alignment in the vicinity of Fermi level have no drastic changes with respect to the fully decoupled case presented in Fig. 1(b). The exchange gap decreases by a few meV due to a slight downward shift of the upper part of the cone; the change in the energy of the Rashba states is also small, but their momentum splitting is halved compared to a freestanding BiTeI trilayer [Figs. 1(c) and 3(a)]. However, this weak interaction induces a large ∼0.4 eV upward shift of spin-orbit split trivial surface states [marked by the T symbol in Fig. 3(a)] residing at −0.65 eV in the case of pristine MBT [also marked by T in Fig. 1(b)]. Moreover, the sign of effective masses of these spin split states is switched (see also Fig. 2 of Ref. [44]).

When the spacing becomes 0.3 Å greater than the equilibrium one ($\Delta d = d - d_0 = 0.3$ Å), the trivial surface state transforms to a cone with helical spin polarization whose apex lies at the energy of −0.11 eV, at that, the increasing

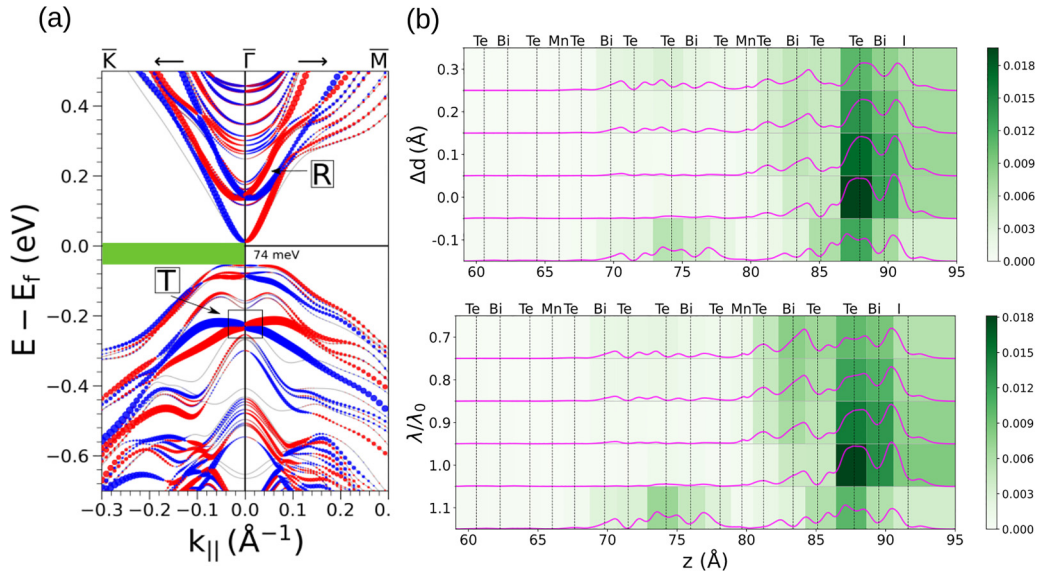

FIG. 3. (a) *In-plane* spin-resolved surface electronic structure of Te-Te interface with a vertical separation $d = 3.24$ Å. (b) Charge density distribution of the upper part of the Dirac surface state (purple curves) at the $\overline{\Gamma}$ point as function of out-of-plane direction (integrated over the *xy* plane) for different vertical spacing between the MBT surface and trilayer (top) and spin-orbit coupling strength, λ/λ_0 (bottom) (see also Fig. 2). The integral of charge density inside the vicinity of adjoined atomic layers are color-coded by the intensities of green.

interaction within the interface tends to relocate the wave function from the magnetic septuple layer to the trilayer. The flattened lower part of the Dirac cone acquires a sharp shape around the $\overline{\Gamma}$ point with the same helicity as the modified trivial surface state. In contrast, the Rashba state relocates from the trilayer to the underlying septuple block of the MBT substrate, and its momentum splitting crucially declines [see Fig. 2(a)].

At further reduction of Δd, the cone of the trivial surface state moves up, passes through the valence band, and in the region of the SBZ center hybridizes with the flat lower part of the Dirac cone, which keeps its energy position beyond the $\overline{\Gamma}$-point vicinity [Figs. 2(b) and 2(c)]. At equilibrium distance, $d = d_0$, the formation of an almost gapless Dirac state is revealed, which is hybridized with the bulk bands near the SBZ center forming a set of surface resonances, and the apex of the lower cone reaches the maximum energy at the $\overline{\Gamma}$ point [Fig. 1(d)]. The subsequent shrinking of the interlayer distance, d, shifts the topological surface states down in the energy scale [Fig. 2(d)], albeit the exchange gap size is still negligible. Note that the TSS wave function tends to be localized in the trilayer when approaching to MBT similar to the case of BiTeI/Au(111) interface [50]. However, under compression of the interface, the TSS pulls back into the subsurface region (see lower curves of the top panel in Fig. 3(b)) due to the resonant character of this state when the magnetic exchange gap lies in the spectral region of the bulk state projection of the highest valence band.

The distance dependent surface electronic structure evolves in a similar way as it happens at artificial SOC modulation on Bi and Te atoms of the trilayer [see Figs. 2(e)–2(h)]. Increasing the interlayer distance by $\Delta d = 0.1$ Å, surface states shift in a similar fashion as the reduction of the SOC factor by 10%, $\lambda/\lambda_0 = 0.9$ [Figs. 2(c) and 2(g)]. Note that it is enough to modulate the SOC factor of p states only, since the TSS are predominantly composed by this type of orbitals. Finally, under compression, $\Delta d = -0.1$ Å [Fig. 2(d)] or at increased SOC factor, $\lambda/\lambda_0 = 1.1$, the lower part of the cone shifts down in the energy scale [Fig. 2(h)]. Moreover, the wave function of the upper part of cone is maximally localized on the trilayer at equilibrium distance and natural SOC strength, $\lambda/\lambda_0 = 1$. With increasing λ/λ_0, the Dirac cone charge localization is extruded back to the MBT in the same way as at approaching BiTeI trilayer close to MBT surface [see the lower curve of the bottom panel of Fig. 3(b)], which, again, is the result of the resonant character of the Dirac cone state near the SBZ center.

The effect described just above originates from the antiparallel directed trilayer dipole moment, which induces a potential gradient on the MBT surface. The same has been previously observed under additional surface doping [48] when the surface negative charge reduces the exchange gap in pristine MBT [48], due to downshift of the upper part of the split Dirac cone. Such a relationship of spin-orbit interaction and electric field effects has been revealed in various materials [56–58].

For this type termination, the formation of the exchange gap in the Dirac state is the source of a range of transport phenomena: half-quantized Hall conductivity [59], anomalous Hall effect [22,60], and topological magnetoelectric effect [61,62].

B. Te–I interface

The inverted polarity of the trilayer in the Te-I interface leads to the parallel orientation of the dipole moment of this building block with respect to the MBT surface normal. It provides a positive potential gradient near the vacuum region. Hence, at approaching of the trilayer closer to the MBT surface, the Dirac state reallocates inside the trilayer. Such an effect of TSS redistribution towards the vacuum boundary has

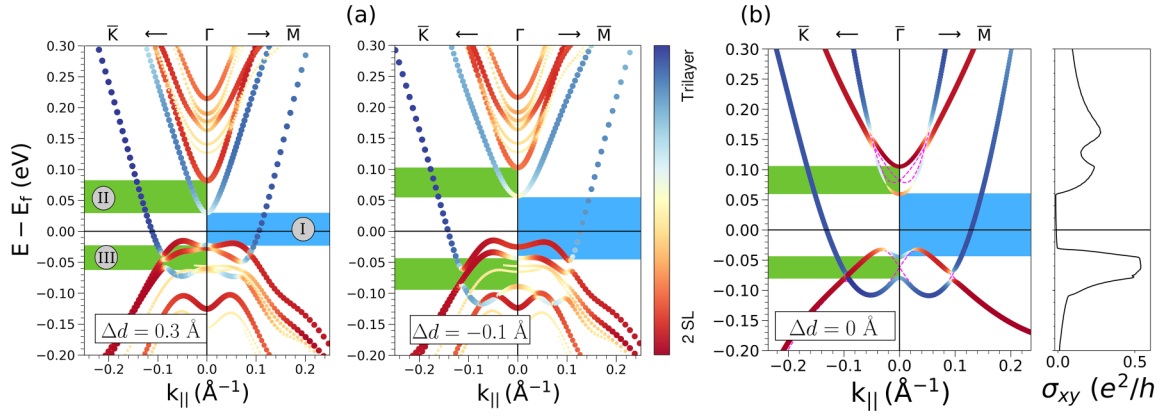

FIG. 4. Surface electronic structure of Te-I interface for different spacings between the BiTeI overlayer and MBT surface. (a) The spacing is 0.3 Å greater (left) and 0.1 Å lesser (right) than the equilibrium one. The colors highlight the extent of spacial localization of the states inside the trilayer (blue) or within the two utmost septuple layers of MBT (red). (b) Electronic band structure [Eq. (1)] of the proposed model (left) with parameters given in Table I (solid black lines) and without taking into account the magnetic contribution, $\hat{H}_m$ ($\Delta_R = \Delta_D = 0$) (dashed red lines). (Right) Energy dependence of Hall conductivity $\sigma_{xy}(E) = V/(2\pi)^2 \int d^2\mathbf{k}\sigma_{xy}(\mathbf{k}, E)$. For all panels, the magnetic exchange and hybridization energy gap at the center of SBZ are denoted by green (blue) areas. Hybridization energy gap is denoted as I and two exchange gaps as II and III.

been previously observed in the case of MBT surfaces under a positive external electric field [48]. Also, in the case of the Te-I interface as Δd decreases the Rashba-type state moves down in the spectrum. In such a way, at $\Delta d = 1$ Å, this state overlaps with the lower part of the Dirac cone immediately below the Fermi level with the formation of hybridization between them. It manifests the single four-band composite state that persists at subsequent decrease of Δd.

In Fig. 4(a), the corresponding spectra are shown for $\Delta d = 0.3$ Å (left panel) and $\Delta d = -0.1$ Å (right panel). Decreasing the distance between the trilayer and the MBT surface affects the width of local band gaps of different nature. Over this process, the hybridization gap (marked as I on the figure) is becoming larger (from 57 meV at $\Delta d = 0.3$ Å, up to 100 meV at $\Delta d = -0.1$ Å), which agrees with enhancing the interaction between building blocks. At the same time, local exchange gaps (II, III) behave differently. The unoccupied one is shrinking from 52 meV ($\Delta d = 0.3$ Å) to 45 meV ($\Delta d = -0.1$ Å), while the occupied one, on the contrary, enlarges from 34 to 46 meV. Such an effect speaks for the complexity of the interaction between hybridization and exchange contribution for this four-band state. Another effect of the complex hybridization of Rashba-type and Dirac states is expressed in spectra by changing the character of the contribution in the vicinity of the $\overline{\Gamma}$ point for the hybridization gap edges. The unoccupied branch is composed by the Dirac state contribution, which corresponds to the localization within the two upper SL blocks (2SL), while the occupied one is formed by the Rashba-type contribution (localized within the trilayer block). Out of the SBZ center, the contribution becomes inverted, i.e., the unoccupied band is contributed by the trilayer block, while the occupied one by the 2SL blocks. It should be noted, the exchange nature of gaps II and III is manifested in the formation of S_z spin component for all involved four bands of the considered composite state (see also Fig. 4(a) in Ref. [44]).

TABLE I. Parameters of the four-band model (1), obtained from the fitting *ab initio* band spectrum.

	$\mu = D$	$\mu = R$		$\mu = D$	$\mu = R$
M_0^μ (eV)	0.05	−0.02	α_μ(eV Å)	1.42	−1.90
M_1^μ (eVÅ^2)	2.29	15.66	γ_μ(eVÅ^3)	11.85	26.67
Δ_μ (eV)	0.035	0.010	A (eV)	0.06	

To address the transport properties of the composite four-band surface state at Te-I interface, we use the simple $\mathbf{k}\cdot\mathbf{p}$ model. The model Hamiltonian (1) is composed by two contributions. The first one describes the linear Dirac-type states and Rashba-type states interaction, the second one the time-reversal symmetry breaking magnetic contribution, $\hat{H}_m$:

$$\hat{H}(\mathbf{k}) = \begin{pmatrix} \hat{H}^D(\mathbf{k}) & \hat{H}_{\text{int}} \\ \hat{H}_{\text{int}}^\dagger & \hat{H}^R(\mathbf{k}) \end{pmatrix} - \hat{H}_m. \tag{1}$$

Here, $\hat{H}^D(\mathbf{k})$ and $\hat{H}^R(\mathbf{k})$ are 2×2 Hamiltonians of the Dirac and Rashba-type states localized in the uppermost seven-layer block of the substrate and BTI overlayer, respectively. Both contributions have the same form, distinguished only by the parameter values:

$$\hat{H}^\mu(\mathbf{k}) = M_0^\mu + M_1^\mu k^2 + \alpha_\mu(k_x\hat{\sigma}_y - k_y\hat{\sigma}_x) + \frac{\gamma_\mu}{2}(k_+^3 + k_-^3)\hat{\sigma}_z,$$

where $\hat{\sigma}$ are Pauli matrices in spin space, μ identifies the Dirac (D) or Rashba (R) part of the Hamiltonian, M_0^μ and M_1^μ are the constant-energy shift and kinetic energy strength contributions, respectively. α_μ and γ_μ are the spin-orbit and hexagonal warping strengths, respectively [63]. The hybridization contribution $\hat{H}_{\text{int}}$ does not depend on momentum and takes the form $A\sigma_0$. The magnetic term is defined by $\hat{H}_m = \text{diag}(\Delta_D, -\Delta_D, \Delta_R, -\Delta_R)$, where Δ_μ is the strength of the Zeeman contribution with an out-of-plane magnetic moment. It should be noted that the proposed model is relevant within the small area near the $\overline{\Gamma}$ point, where possible

higher-order terms are caused by the impact of another nearby surface and resonant states. The parameters of the Hamiltonian have been obtained via the fitting procedure applied to the *ab initio* surface spectrum, and are shown in the Table I. The Rashba-type part $\hat{H}_R(\mathbf{k})$ has a dominant kinetic energy term, M_1^R, with respect to the spin-orbit contribution strength, α_R, and has opposite sign with respect to the one of $H_D(\mathbf{k})$. The relative difference between exchange parameters Δ_R and $\Delta_D(\Delta_D/\Delta_R = 3.5)$ in the Rashba-type state and linear Dirac state is in good accordance with aspects of localization of these states: the former is located mostly in the trilayer block, while the latter in the uppermost seven-layer block of the magnetic substrate.

On the left panel of Fig. 4(b), the energy spectrum of the presented model is shown for the parameters given in Table I (color-coded curves), and for these parameters, but without the magnetic contribution, $\Delta_D = \Delta_R = 0$ (red dashed lines). The bright feature of the presented spectra is the hybridization band gap near the $\overline{\Gamma}$ point, at -0.02—0.05 eV energy range [Fig. 4(a)], which is formed by nonzero A, and this aspect of the model exactly reproduces the *ab initio* results. As can be seen in the figure, the magnetism enhances the range of features in the spectrum. Firstly, it produces local exchange gaps in the vicinity of the $\overline{\Gamma}$ point at ~ -0.08 and $\sim$0.1 eV (green color on the figure), which is also in agreement with the *ab initio* results. Secondly, it is avoided crossings: at ~ -0.08 eV, they are located along $\overline{\Gamma}$-$\overline{\mathrm{K}}$ direction, while along $\overline{\Gamma}$-$\overline{\mathrm{M}}$ such features are also caused by the additional hexagonal warping effect. At $\sim$0.15 eV, the formation of this type of features is artificial, owing to the limitation of the $\mathbf{k}\cdot\mathbf{p}$ model producing the intersection of Rashba-type and the linear Dirac state branches without magnetism.

Both time reversal symmetry breaking and surface inversion asymmetry induce nonzero Hall conductivity. On the right panel of Fig. 4(b), we show the energy dependence of Hall conductivity, σ_{xy}, integrated over momentum space at each E. The Hall conductivity has been calculated by using the antisymmetric component of topological Berry curvature tensor $\Omega_n^{xy}(k)$:

$$\sigma_{xy}(\mathbf{k}, E) = \frac{e^2}{h}\sum_n f(E_n - E)\Omega_{xy}^n(\mathbf{k}),$$

where f is the Fermi function, and $\Omega_n^{xy}(\boldsymbol{k})$ has been computed by using the Kubo formula:

$$\Omega_{xy}^n(\mathbf{k}) = 2\hbar^2 \mathrm{Im}\sum_{\mathrm{n}'\neq\mathrm{n}} \frac{\langle \mathrm{n}|\hat{\mathrm{v}}_\mathrm{x}|\mathrm{n}'\rangle\langle \mathrm{n}'|\hat{\mathrm{v}}_\mathrm{y}|\mathrm{n}\rangle}{[\mathrm{E_n} - \mathrm{E_{n'}}]^2},$$

where the velocity operators are $\hat{\mathrm{v}}_{x,y} = 1/\hbar\,\partial\hat{H}/\partial k_{x,y}$.

The maximal intensity is located at the energy where the magnetic contribution into the band dispersion is maximal, i.e., the regions of the exchange gaps and avoided crossings. The bright peak of $\sigma_{xy}(E)$ is located at -0.08 eV, decaying down to the energy scale. At energy range of 0.08–0.18 eV, a two-peak feature is shown, where the lower peak corresponds to the exchange gap at the $\overline{\Gamma}$ point and the higher the discussed avoided crossing feature. In such a way, there are two energy areas contributing to the Hall conductivity, and they correspond to the local band gaps of lifted Kramers degeneracies due to the magnetism.

IV. CONCLUSION

In the case of Te-Te interface of a MBT/BTI heterostructure, the effect of the presence of the overlayer induces a spatial shift of the exchange split Dirac cone into the region of the BiTeI overlayer and in reducing of the exchange gap size with respect to pristine surface of the substrate. As a result, the surface Dirac cone mostly locates inside the polar overlayer despite that the Rashba-type spin splitting is a spectral peculiarity of the BiTeI compound. Such an effect is related with bulk gap edge states inversion of the substrate, which has been also demonstrated via the *ab initio* calculations. In such a way, the deposition of BiTeI trilayer on the $MnBi_2Te_4$ surface can be the route to manipulation of exchange gap size of the Dirac cone.

Between two possible side surfaces of MBT/BTI interfaces, the Te-Te case stands out by the formation of a four-band state induced by the Rashba-type and linear Dirac cone coupling. Owing to the magnetic nature of the substrate, this state undergoes sizable exchange splitting, which ensures intrinsic Hall conductivity contribution via the time-reversal symmetry breaking. Herewith, the observed conductivity is not quantized due to nonzero density of states in the corresponding energy region. The described properties of the four-band state resemble those of the widely studied exchange-split Rashba-type state, which is a useful model to study fundamental aspects of anomalous Hall conductivity [11]. Hence, one can expect the same magnetotransport phenomena for the described four-band state of the current investigation. First of all, additional random impurities should produce extrinsic side-jump and skew-scattering contributions to anomalous Hall conductivity in the Te-I interface of the MBT/BTI heterostructure [64–66]. Next, one can expect the surface anisotropic magnetoresistance effect [67,68]. Due to the strong spin-orbit coupling contribution of the BiTeI overlayer, Dzyaloshinskii-Moriya spin interaction can be produced, which ensures the formation of skyrmions and magnetic domain walls [69], which opens the way for manipulation of spin momentum of electrons based on the recently proposed chiral orbital magnetization effect [9]. Another type of related photovoltaic and optical effects in the proposed system are the photocurrent at zero-bias voltage [70–72] and topological Kerr effect [73,74]. In the proximity of a superconductor, it can possible create Majorana fermion states [75,76], which allows one to apply the proposed heterostructure in quantum computation [12]. We note that the considered four-band state can be more advantageous with respect to the Rashba-type state, owing to the presence of two wide energy ranges with contribution of Hall conductivity. As a result, the Fermi level can be easily pinned at this energy regions via the surface doping.

ACKNOWLEDGMENTS

E.V.C. acknowledges support from Saint Petersburg State University (Grant No. ID 90383050). N.L.Z., I.P.R., acknowledge support from Russian Science Foundation within Research Project No. 18-12-00169-p (in the part of DFT calculation of equilibrium Te-Te and Te-I interfaces). T.V.M. acknowledges support from the Ministry of Education and

Science of the Russian Federation within State Task No. FSWM-2020-0033 (in the part of interface geometry relaxation and electronic structure calculation of Te-Te contact with different MBT and TL spacing).

[1] D. N. Basov, R. D. Averitt, and D. Hsieh, Nat. Mater. **16**, 1077 (2017).

[2] Y. Tokura, K. Yasuda, and A. Tsukazaki, Nat. Rev. Phys. **1**, 126 (2019).

[3] T. Jungwirth, X. Marti, P. Wadley, and J. Wunderlich, Nat. Nanotechnol. **11**, 231 (2016).

[4] G. Bihlmayer, O. Rader, and R. Winkler, New J. Phys. **17**, 050202 (2015).

[5] Y. A. Bychkov and E. I. Rashba, JETP Lett. **39**, 78 (1984).

[6] S. Datta and B. Das, Appl. Phys. Lett. **56**, 665 (1990).

[7] I. Žutić, J. Fabian, and S. Das Sarma, Rev. Mod. Phys. **76**, 323 (2004).

[8] M. Z. Hasan and C. L. Kane, Rev. Mod. Phys. **82**, 3045 (2010).

[9] F. R. Lux, F. Freimuth, S. Blügel, and Y. Mokrousov, Commun. Phys. **1**, 60 (2018).

[10] A. Manchon, J. Železný, I. M. Miron, T. Jungwirth, J. Sinova, A. Thiaville, K. Garello, and P. Gambardella, Rev. Mod. Phys. **91**, 035004 (2019).

[11] N. Nagaosa, J. Sinova, S. Onoda, A. H. MacDonald, and N. P. Ong, Rev. Mod. Phys. **82**, 1539 (2010).

[12] C. Nayak, S. H. Simon, A. Stern, M. Freedman, and S. Das Sarma, Rev. Mod. Phys. **80**, 1083 (2008).

[13] S. R. Elliott and M. Franz, Rev. Mod. Phys. **87**, 137 (2015).

[14] K. S. Novoselov, K. Mishchenko, A. Carvalho, and A. H. Castro Neto, Science **353**, aac9439 (2016).

[15] A. K. Geim and I. V. Grigorieva, Nature (London) **499**, 419 (2013).

[16] H. Qi, L. Wang, J. Sun, Y. Long, P. Hu, F. Liu, and X. He, Crystals **8**, 35 (2018).

[17] M. M. Otrokov, I. I. Klimovskikh, H. Bentmann, D. Estyunin, A. Zeugner, Z. S. Aliev, S. Gaß, A. U. B. Wolter, A. V. Koroleva, A. M. Shikin *et al.*, Nature (London) **576**, 416 (2019).

[18] E. D. L. Rienks, S. Wimmer, J. Sánchez-Barriga, O. Caha, P. S. Mandal, J. Růžička, A. Ney, H. Steiner, V. V. Volobuev, H. Groiss *et al.*, Nature (London) **576**, 423 (2019).

[19] M. M. Otrokov, T. V. Menshchikova, M. G. Vergniory, I. P. Rusinov, A. Y. Vyazovskaya, Y. M. Koroteev, G. Bihlmayer, A. Ernst, P. M. Echenique, A. Arnau *et al.*, 2D Mater. **4**, 025082 (2017).

[20] M. M. Otrokov, I. P. Rusinov, M. Blanco-Rey, M. Hoffmann, A. Y. Vyazovskaya, S. V. Eremeev, A. Ernst, P. M. Echenique, A. Arnau, and E. V. Chulkov, Phys. Rev. Lett. **122**, 107202 (2019).

[21] R. C. Vidal, H. Bentmann, T. R. F. Peixoto, A. Zeugner, S. Moser, C.-H. Min, S. Schatz, K. Kißner, M. Ünzelmann, C. I. Fornari *et al.*, Phys. Rev. B **100**, 121104(R) (2019).

[22] Y. Deng, Y. Yu, M. Z. Shi, Z. Guo, Z. Xu, J. Wang, X. H. Chen, and Y. Zhang, Science **367**, 895 (2020).

[23] D. Zhang, M. Shi, T. Zhu, D. Xing, H. Zhang, and J. Wang, Phys. Rev. Lett. **122**, 206401 (2019).

[24] S. V. Eremeev, I. A. Nechaev, Y. M. Koroteev, P. M. Echenique, and E. V. Chulkov, Phys. Rev. Lett. **108**, 246802 (2012).

[25] K. Ishizaka, M. S. Bahramy, H. Murakawa, M. Sakano, T. Shimojima, T. Sonobe, K. Koizumi, S. Shin, H. Miyahara, A. Kimura *et al.*, Nat. Mater. **10**, 521 (2011).

[26] A. Liang, C. Chen, H. Zheng, W. Xia, K. Huang, L. Wei, H. Yang, Y. Chen, X. Zhang, X. Xu *et al.*, Nano Lett. **22**, 4307 (2022).

[27] X.-M. Ma, Z. Chen, E. F. Schwier, Y. Zhang, Y.-J. Hao, S. Kumar, R. Lu, J. Shao, Y. Jin, M. Zeng *et al.*, Phys. Rev. B **102**, 245136 (2020).

[28] D. S. Lee, T.-H. Kim, C.-H. Park, C.-Y. Chung, Y. S. Lim, W.-S. Seo, and H.-H. Park, CrystEngComm **15**, 5532 (2013).

[29] M. Otani and O. Sugino, Phys. Rev. B **73**, 115407 (2006).

[30] S. Grimme, S. Ehrlich, and L. Goerigk, J. Comput. Chem. **32**, 1456 (2011).

[31] S. Grimme, J. Antony, S. Ehrlich, and H. Krieg, J. Chem. Phys. **132**, 154104 (2010).

[32] G. Kresse and D. Joubert, Phys. Rev. B **59**, 1758 (1999).

[33] P. E. Blöchl, Phys. Rev. B **50**, 17953 (1994).

[34] G. Kresse and J. Furthmüller, Comput. Mater. Sci. **6**, 15 (1996).

[35] S. Steiner, S. Khmelevskyi, M. Marsmann, and G. Kresse, Phys. Rev. B **93**, 224425 (2016).

[36] E. v. Lenthe, E. J. Baerends, and J. G. Snijders, J. Chem. Phys. **99**, 4597 (1993).

[37] T. Ozaki, H. Kino, J. Yu, M. Han, N. Kobayashi, M. Ohfuti, F. Ishii, T. Ohwaki, H. Weng, and K. Terakura, http://openmx-square.org/.

[38] T. Ozaki and H. Kino, Phys. Rev. B **69**, 195113 (2004).

[39] T. Ozaki and H. Kino, Phys. Rev. B **72**, 045121 (2005).

[40] T. Ozaki, Phys. Rev. B **67**, 155108 (2003).

[41] N. Troullier and J. L. Martins, Phys. Rev. B **43**, 1993 (1991).

[42] G. Theurich and N. A. Hill, Phys. Rev. B **64**, 073106 (2001).

[43] J. P. Perdew, K. Burke, and M. Ernzerhof, Phys. Rev. Lett. **77**, 3865 (1996).

[44] See Supplemental Material at http://link.aps.org/supplemental/10.1103/PhysRevB.107.045402 for relaxed crystal structure of the interfaces, In-plane spin-resolved surface electronic structure of Te-Te interface with different vertical separation, slab thikness, surface electronic structure of Te-I interface in the case of in-plane and out-of-plane magnetization direction.

[45] S. V. Eremeev, S. S. Tsirkin, I. A. Nechaev, P. M. Echenique, and E. V. Chulkov, Sci. Rep. **5**, 12819 (2015).

[46] S. V. Eremeev, M. G. Vergniory, T. V. Menshchikova, A. A. Shaposhnikov, and E. V. Chulkov, New J. Phys. **14**, 113030 (2012).

[47] A. M. Shikin, D. A. Estyunin, I. I. Klimovskikh, S. O. Filnov, E. F. Schwier, S. Kumar, K. Miyamoto, T. Okuda, A. Kimura, K. Kuroda *et al.*, Sci. Rep. **10**, 13226 (2020).

[48] A. M. Shikin, D. A. Estyunin, N. L. Zaitsev, D. Glazkova, I. I. Klimovskikh, S. O. Filnov, A. G. Rybkin, E. F. Schwier, S. Kumar, A. Kimura *et al.*, Phys. Rev. B **104**, 115168 (2021).

[49] Y.-J. Hao, P. Liu, Y. Feng, X.-M. Ma, E. F. Schwier, M. Arita, S. Kumar, C. Hu, R. Lu, M. Zeng *et al.*, Phys. Rev. X **9**, 041038 (2019).

[50] N. L. Zaitsev, R. Tonner, and I. A. Nechaev, J. Phys.: Condens. Matter **31**, 204001 (2019).
[51] T. c. v. Rauch, M. Flieger, J. Henk, I. Mertig, and A. Ernst, Phys. Rev. Lett. **112**, 016802 (2014).
[52] E. K. Petrov, V. N. Men'shov, I. P. Rusinov, M. Hoffmann, A. Ernst, M. M. Otrokov, V. K. Dugaev, T. V. Menshchikova, and E. V. Chulkov, Phys. Rev. B **103**, 235142 (2021).
[53] D. Pacilè, S. V. Eremeev, M. Caputo, M. Pisarra, O. De Luca, I. Grimaldi, J. Fujii, Z. S. Aliev, M. B. Babanly, I. Vobornik *et al.*, Phys. Status Solidi RRL **12**, 1800341 (2018).
[54] K. D. Rasamani, F. Alimohammadi, and Y. Sun, Mater. Today **20**, 83 (2017).
[55] J. Xu, J. Zhang, W. Zhang, and C.-S. Lee, Adv. Energy Mater. **7**, 1700571 (2017).
[56] L. Chen, M. Gmitra, M. Vogel, R. Islinger, M. Kronseder, D. Schuh, D. Bougeard, J. Fabian, D. Weiss, and C. H. Back, Nat. Electron. **1**, 350 (2018).
[57] D. Maryenko, M. Kawamura, A. Ernst, V. K. Dugaev, E. Y. Sherman, M. Kriener, M. S. Bahramy, Y. Kozuka, and M. Kawasaki, Nat. Commun. **12**, 3180 (2021).
[58] W. Lin, L. Li, F. Doğan, C. Li, H. Rotella, X. Yu, B. Zhang, Y. Li, W. S. Lew, S. Wang *et al.*, Nat. Commun. **10**, 3052 (2019).
[59] X.-L. Qi, T. L. Hughes, and S.-C. Zhang, Phys. Rev. B **78**, 195424 (2008).
[60] M. Mogi, T. Nakajima, V. Ukleev, A. Tsukazaki, R. Yoshimi, M. Kawamura, K. S. Takahashi, T. Hanashima, K. Kakurai, T. H. Arima *et al.*, Phys. Rev. Lett. **123**, 016804 (2019).
[61] J. Wang, B. Lian, X.-L. Qi, and S.-C. Zhang, Phys. Rev. B **92**, 081107(R) (2015).
[62] H.-G. Zirnstein and B. Rosenow, physica status solidi (b) **257**, 1900698 (2020).
[63] L. Fu, Phys. Rev. Lett. **103**, 266801 (2009).
[64] I. A. Ado, I. A. Dmitriev, P. M. Ostrovsky, and M. Titov, Phys. Rev. Lett. **117**, 046601 (2016).
[65] V. K. Dugaev, P. Bruno, M. Taillefumier, B. Canals, and C. Lacroix, Phys. Rev. B **71**, 224423 (2005).
[66] S. Onoda, N. Sugimoto, and N. Nagaosa, Phys. Rev. Lett. **97**, 126602 (2006).
[67] N. Wadehra, R. Tomar, R. M. Varma, R. K. Gopal, Y. Singh, S. Dattagupta, and S. Chakraverty, Nat. Commun. **11**, 874 (2020).
[68] M. Trushin, K. Výborný, P. Moraczewski, A. A. Kovalev, J. Schliemann, and T. Jungwirth, Phys. Rev. B **80**, 134405 (2009).
[69] P. M. Sass, J. Kim, D. Vanderbilt, J. Yan, and W. Wu, Phys. Rev. Lett. **125**, 037201 (2020).
[70] N. Ogawa, R. Yoshimi, K. Yasuda, A. Tsukazaki, M. Kawasaki, and Y. Tokura, Nat. Commun. **7**, 12246 (2016).
[71] A. Fedorov, Y. V. Pershin, and C. Piermarocchi, Phys. Rev. B **72**, 245327 (2005).
[72] Y. V. Pershin and C. Piermarocchi, Appl. Phys. Lett. **86**, 212107 (2005).
[73] D. Bang, H. Awano, J. Tominaga, A. V. Kolobov, P. Fons, Y. Saito, K. Makino, T. Nakano, M. Hase, Y. Takagaki *et al.*, Sci. Rep. **4**, 5727 (2014).
[74] M. Buchner, P. Högl, S. Putz, M. Gmitra, S. Günther, M. A. W. Schoen, M. Kronseder, D. Schuh, D. Bougeard, J. Fabian *et al.*, Phys. Rev. Lett. **117**, 157202 (2016).
[75] M. Sato, Y. Takahashi, and S. Fujimoto, Phys. Rev. Lett. **103**, 020401 (2009).
[76] M. Sato and S. Fujimoto, Phys. Rev. B **79**, 094504 (2009).